Experimental and Theoretical Research on the Corrosion Resistance of Ferrous Alloys in Aluminum Melts

GAOPENG XU, KUI WANG, XIANPING DONG, HAIYAN JIANG, QUDONG WANG, BING YE, and WENJIANG DING

The resistance of three ferrous alloys (HT150, QT500, and H13) to corrosion caused by exposure to aluminum melts has been systematically studied using experiments and modeling. Results show that the exfoliation and dissolution of intermetallic compounds like Fe_2Al_5 and $FeAl_3$ formed by the interdiffusion between aluminum melts and ferrous alloys are responsible for the corrosive attack. Based on the thermodynamics and kinetics of intermetallic compounds, an analytical model has been established to quantitatively account for the corrosion behavior between the ferrous alloys and aluminum melts, and the diffusion inhibition factor λ is first introduced in this work to quantitatively estimate the extent to which the existence of carbon can influence the diffusion of aluminum melts to the ferrous alloys. Theoretical analysis demonstrates that the flake graphite in HT150 can reduce the corrosion rate most effectively, followed by spheroidal graphite in QT500. Both outperform H13.

I. INTRODUCTION

DURING the fabrication and processing of aluminum including melting,[1] forming,[2] and hot dip aluminizing,[3,4] many metal components are immersed into aluminum melts. They are often subjected to severe corrosion, which in turn shortens their service lives and results in the contamination of aluminum melts, degrading the efficiency of aluminum processing and product quality.[5,6] Although refractory metals, such as Nb, Mo, W, Co, and their alloys, have excellent resistance to aluminum corrosion,[7–[1]] they are costly and difficult to synthesize, greatly limiting their applications. To minimize the corrosion of metal components, the demand for low-cost metal materials with high corrosion resistance has become increasingly urgent in the field of aluminum processing.

Gray cast iron is commonly used for tooling and structural components required for processing of aluminum melts due to excellent corrosion resistance, easy molding, and low cost. However, it has low strength at high temperature and is easily oxidized to cause growth cracking. Alloying is usually utilized to improve its comprehensive property. Conversely, ductile iron has poor corrosion resistance, but good resistance to thermal fatigue and oxidation. It is widely used in the production of hot-worked aluminum.[12] Additionally, the corrosion resistance of H13 is poor as well, but has excellent thermal stability, high temperature strength, wear resistance, thermal fatigue resistance, and oxidation resistance.[13] As a result, it is often used as aluminum alloy die-casting mold and extrusion die. Nevertheless, the ferrous alloys mentioned above are inevitably subjected to different degree of corrosion when applied in aluminum melt environment.

The reactions between aluminum melts and ferrous alloys can lead to the formation of different intermetallic compounds (IMCs). However, not all IMCs can be formed during hot dipping tests. Numerous studies[14–19] show that the ferrous alloy can react with the aluminum melts to form the IMC layer that mainly contains Fe_2Al_5 and $FeAl_3$, and the exfoliation of IMCs can lead to the corrosion of ferrous alloys. Sidhu[14] suggested that the presence of C-rich phases, graphite flakes, and cementite was effective in enhancing the aluminum melt corrosion resistance of gray cast irons, and the graphite morphology can play a pivotal role in aluminum melt corrosion resistance. Balloy et al.[15] also found that the graphite flake is favorable for the diffusion inhibition of Al atoms during the corrosion of the cast iron in aluminum melts. However, the influence mechanisms of the morphology and distribution of graphite and carbide on the

GAOPENG XU, KUI WANG, XIANPING DONG, HAIYAN JIANG, QUDONG WANG, BING YE, and WENJIANG DING are with the National Engineering Research Center of Light Alloy Net Forming and the State Key Laboratory of Metal Matrix Composites, Shanghai Jiao Tong University, Shanghai 200240, P.R. China. Contact e-mail: fateratory@sjtu.edu.cn

corrosion resistance of ferrous alloys still remain not to be fully understood up to now, especially from the perspective of the formation, growth, and nature of Fe-Al IMCs. In addition, few studies have been conducted to elucidate their effects on the diffusion inhibition of Al atoms and the growth restriction of IMCs quantitatively.

In this study, the static aluminum melt corrosion tests were conducted on HT150, QT500, and H13 steels, and the microstructure of reaction layers was analyzed to reveal the effect of chemical composition on the aluminum melt corrosion resistance of ferrous alloys. Based on the thermodynamic kinetics of IMCs, a theoretical model was established to quantitatively estimate the extent to which the existence form of carbon can influence the corrosion rate, which may provide the guidelines for producing the ferrous alloy with enhanced aluminum melt corrosion resistance. A growth-restriction mechanism was then proposed to further understand the corrosion behavior of ferrous alloys in aluminum melts.

II. EXPERIMENTAL MATERIALS AND METHODS

The selected ferrous alloys are HT150, QT500, and H13, and their chemical compositions are shown in Table I. In order to avoid the influence of other elements in the aluminum melts on the corrosion of the alloys, pure aluminum was selected as the etching media.

First of all, experimental alloys were machined into sheet specimens of $80 \times 10 \times 5$ mm. Samples were sanded, ultrasonically cleaned, dried, and then sized with a vernier caliper. The mass of different samples was measured with an analytical balance before the experiment. As shown in Figure 1, samples were immersed into aluminum melts at 1023 K (750 °C) for different lengths of time, taken out, and then cooled in air.

To quantitatively analyze the corrosion depth, the thicknesses of the sample matrix and the IMC layers formed by the interfacial reaction were measured in the cross sections shown in Figure 1, and the thickness loss of the sample matrix (Δx) is given by

$$\Delta x = \frac{x_1 - x_2}{2}, \qquad [1]$$

where x_1 (μm) and x_2 (μm) refer to the thickness of the sample before and after corrosion, respectively.

Table I. Chemical Compositions of the Alloys

Alloy	Main Chemical Compositions (Weight Percent)						
	C	Si	Mn	Cr	V	Mo	Fe
HT150	3.52	1.98	0.71	—	—	—	bal.
QT500	3.63	2.35	0.56	—	—	—	bal.
H13	0.36	0.95	0.32	4.88	1.12	1.39	bal.

Samples were cut along the direction perpendicular to the corrosion surface, sanded with sandpaper, polished, and then etched with 4 pct Nitric acid alcohol solution. The microstructure of each immersed sample was observed by scanning electron microscopy (SEM; VEGA 3 XMU, Czech). Images were obtained using backscattered electron (BSE) mode allowing chemical contrast, and elements in each phase were semi-quantitatively analyzed by XFlash 6130 spectrometer (EDS). The phase identification, phase distribution, and crystal orientation were analyzed using electron backscatter diffraction (EBSD). Phase analysis of reaction products was undertaken by X-ray diffractometer (XRD; Smart Lab, Japan).

III. RESULTS AND DISCUSSION

A. *Phase Analysis and Microstructures*

Figure 2 shows the SEM images of the three ferrous alloys immersed in aluminum melts at 1023 K (750 °C) for 24 hours. Because of the interdiffusion between ferrous alloys and aluminum melts, a distinct intermediate transition layer was formed at the interface between the matrix and the aluminum layer. Figure 2(a) shows the corrosion interface of HT150. Compared with QT500 (Figure 2(b)) and H13 (Figure 2(c)), the corrosion interface of HT150 adjacent to the matrix side is uniform, and the thickness of intermediate transition layer is much smaller than those of QT500 and H13. As shown in the Figure 2(d), the thicknesses of IMC layers in HT150, QT500, and H13 is about 160, 450, and 500 μm, respectively. However, the interfaces between the matrixes and the IMC layers of H13 and QT500 are undulated, and several irregular tongue-shaped phases extend into the interior of the matrix perpendicularly to the interface. Unlike QT500, the interface between the IMC layer of H13 and the aluminum layer is relatively uniform.

Figure 3 illustrates the XRD patterns of the ferrous alloys immersed at 1023 K (750 °C) for 24 hours. Results show that the corrosion products of HT150, QT500, and H13 are mainly composed of Fe_2Al_5 and $FeAl_3$ phases. Since the alloying elements such as Cr and Mo are added to H13, the carbides are also identified in H13.

The interfacial morphology of HT150 immersed in aluminum melts at 1023 K (750 °C) for 24 hours is shown in Figure 4(a). The interface exhibits a typical three-layer structure that consists of the left HT150 matrix, the intermediate IMC layer, and the right aluminum layer. A large amount of flake graphite is distributed throughout the matrix in a form of network. The elements mapping analysis was performed on the local area at the interface, and the selected area is indicated by the yellow box in Figure 4(a). Results show that the intermediate IMC layer is a two-layer structure. The side adjacent to HT150 matrix is a transition layer which occupies the most part of IMC layer, forming an irregular tongue-shaped interface with the matrix. The tip of the tongue grows preferentially towards the
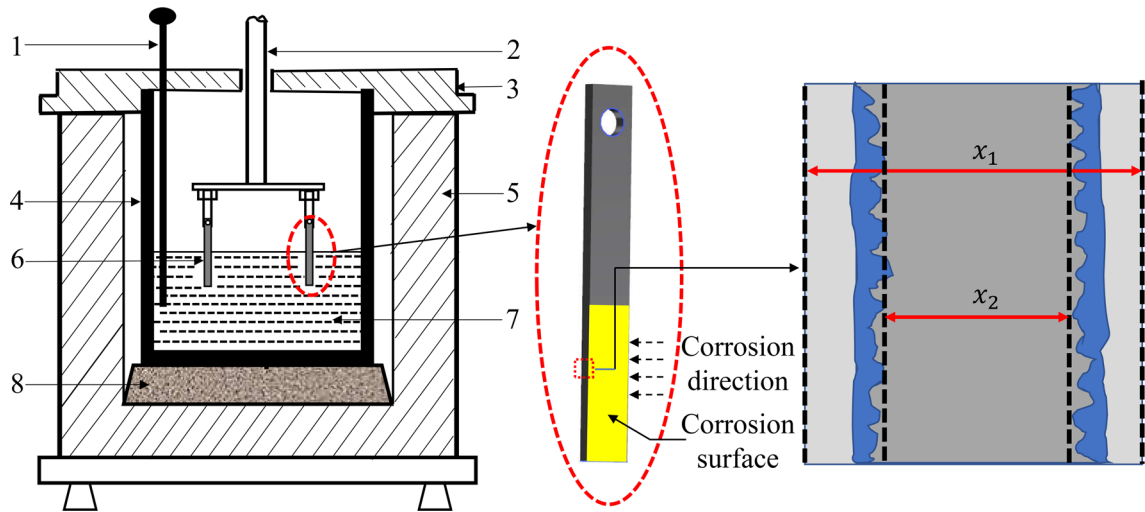
1- Thermocouple; 2- Sample holder; 3- Insulation cover; 4- Crucible; 5- Resistance furnace;

6- Sample; 7- Aluminum melts; 8- Refractory brick

Fig. 1—Schematic of experimental set-up used for the immersion test and measure of the thickness loss.
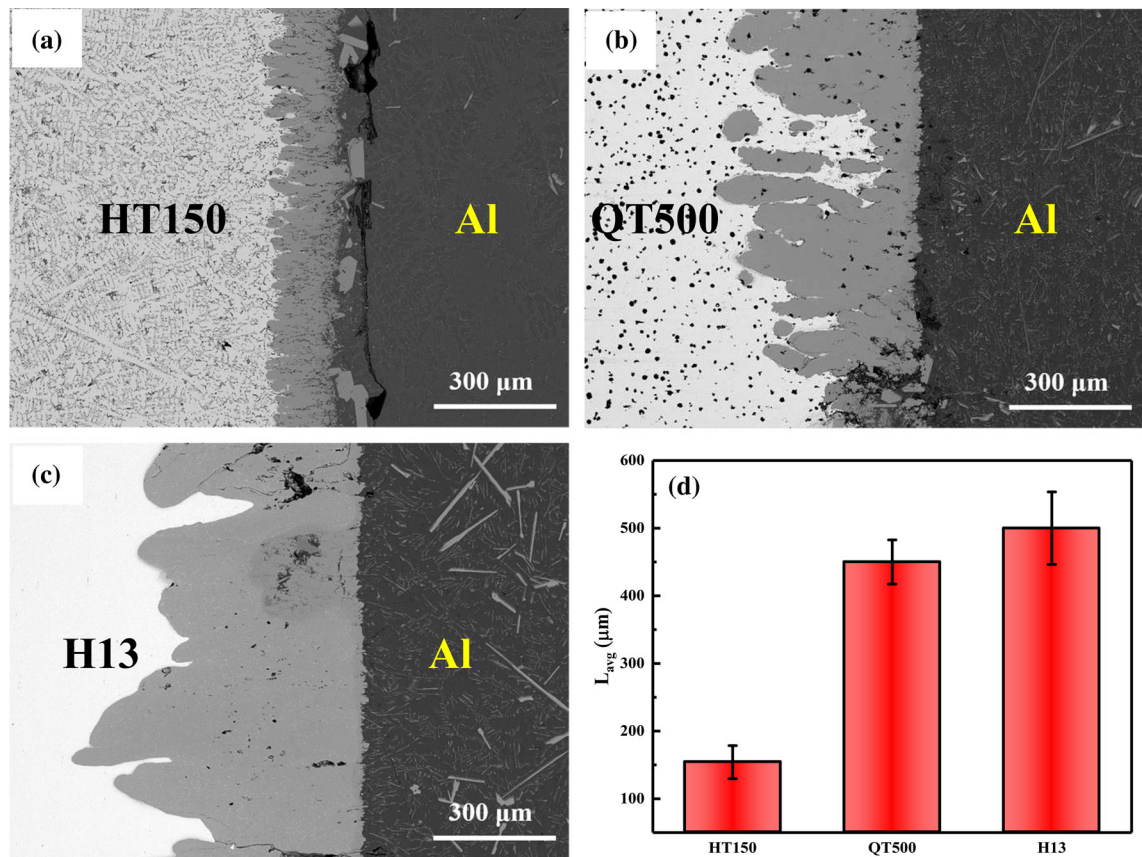

Fig. 2—SEM images of the three ferrous alloys immersed in the aluminum melts at 1023 K (750 °C) for 24 h: (*a*) HT150; (*b*) QT500; (*c*) H13; (*d*) average thickness of IMC layer of the three ferrous alloys.

matrix. In combination with the EDS results (Table II) and EBSD mapping (Figure 5(a)), the transition layer is composed of Fe_2Al_5 phases. Heumann *et al.*[20] suggested that Fe_2Al_5 grew into the matrix in a specific direction caused by the difference in the diffusion coefficients of Fe and Al. The crystal lattice of Fe_2Al_5 is orthogonal structure, and there is a high vacancy concentration in the c-axis direction, which allows Al

atoms to diffuse rapidly along the c-axis direction to the interface front, resulting in the preferential growth of Fe_2Al_5 along the c-axis direction and thus the formation of a tongue-shaped morphology.[3] In this work, the inverse pole figure map of the Fe_2Al_5 IMCs was employed to clarify the crystallographic features of the Fe_2Al_5 layer. As shown in Figure 5(b), the Fe_2Al_5 IMCs exhibit a strongly textured layer with the grains oriented mainly in the [001] direction, which is the c-axis parallel to the normal direction (ND). Therefore, it can be confirmed that the Al atom has the highest diffusion coefficient in Fe_2Al_5 along the c-axis direction. Based on the EDS results (Table III) and EBSD mapping (Figure 5(a)), the layer adjacent to the aluminum layer is composed of $FeAl_3$ formed by the reaction diffusion, and smaller than Fe_2Al_5 layer in thickness. At the interface between $FeAl_3$ and aluminum layer, a large number of broken particles are found to adhere to $FeAl_3$, and many large blocks or strips are attached to

$FeAl_3$ or even freely distributed in the aluminum layer. The chemical compositions of these phases are identical to that of $FeAl_3$. Actually, the formation of $FeAl_3$ adhered to the interface depends not only on reaction diffusion but also on the precipitation of the IMCs, while the free $FeAl_3$ is only formed by precipitation.[21] In addition, the flocculent structures are found in the solidified aluminum layer, as shown in Figure 4(a).

After immersion in aluminum melts at 1023 K (750 °C) for 24 hours, the intermediate transition layer of QT500 is shown in Figure 6(a). Combined with the results of EDS analysis (Figures 6(b) through (e) and Table III) and XRD (Figure 3), it can be seen that the intermediate transition layer is also composed of Fe_2Al_5 growing towards to the matrix and $FeAl_3$ adjacent to the solidified aluminum layer. Unlike HT150, the tongue-shaped Fe_2Al_5 in QT500 is disconnected partially from the IMC layer, and the IMC layer is larger in size than that in HT150. It may be related to the morphology and distribution of graphite in QT500. As shown in Figure 6(a), the spheroidal graphite is detached from the matrix and distributed discretely in the IMC layer and solidified aluminum layer, which seems to contribute less to the diffusion inhibition of Al atoms in the matrix and thus the growth restriction of IMCs than the flake graphite. In the solidified aluminum layer, a large quantity of elongated strip-shaped $FeAl_3$ and flocculent eutectics of $FeAl_3$ and Al are observed as well.
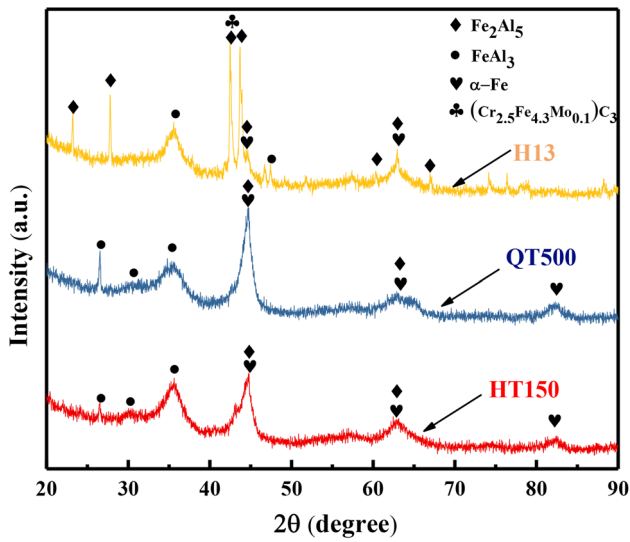

Fig. 3—XRD patterns of corrosion products.

Table II. Chemical Compositions at the Marked Locations in Fig. 4(a)

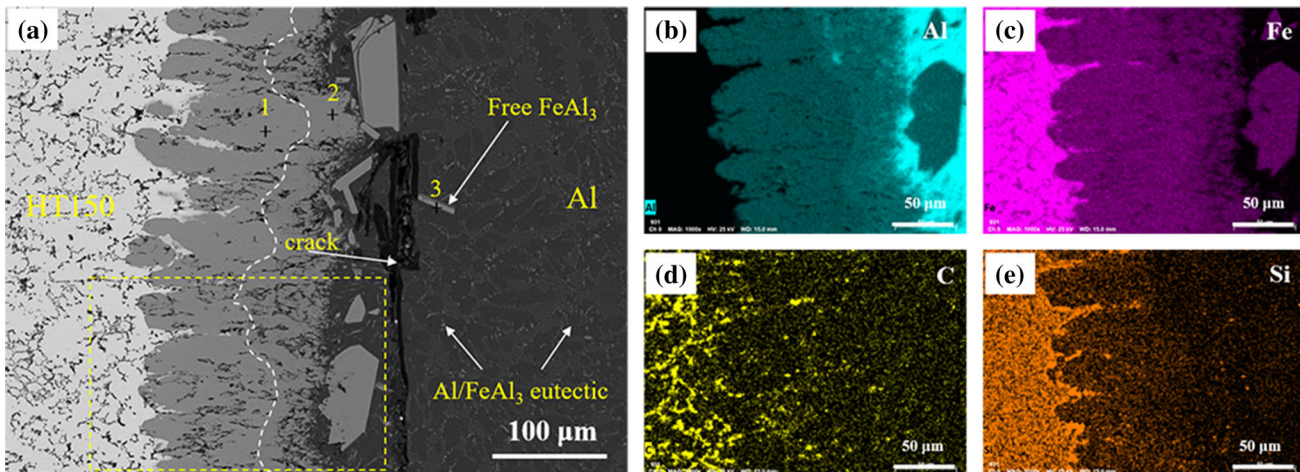| EDS Results (Weight Percent)			
Location	Al	Fe	C	Phase Compositions
1	54.21	41.81	3.97	Fe_2Al_5
2	57.54	40.58	1.88	$FeAl_3$
3	58.91	39.04	2.05	free $FeAl_3$

Fig. 4—SEM images and EDS analysis of the corrosion interface formed in HT150 after 24 h in the aluminum melts at 1023 K (750 °C).
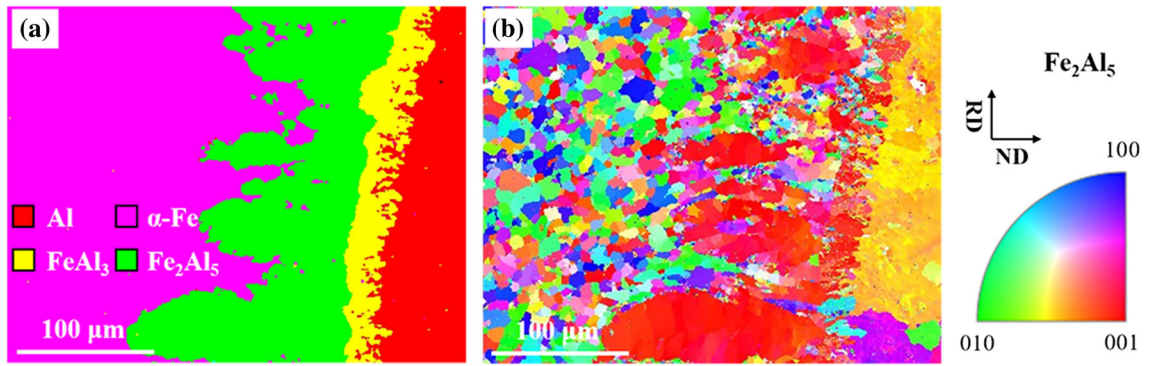
Fig. 5—EBSD analysis of the corrosion interface formed in HT150 after 24 h in the aluminum melts at 1023 K (750 °C): (*a*) the phase distribution map showing the different phases present in the corrosion interface; (*b*) the inversed pole figure map showing the [001] crystallographic direction (parallel to the normal direction) as being the preferred orientation in the Fe_2Al_5 layer.
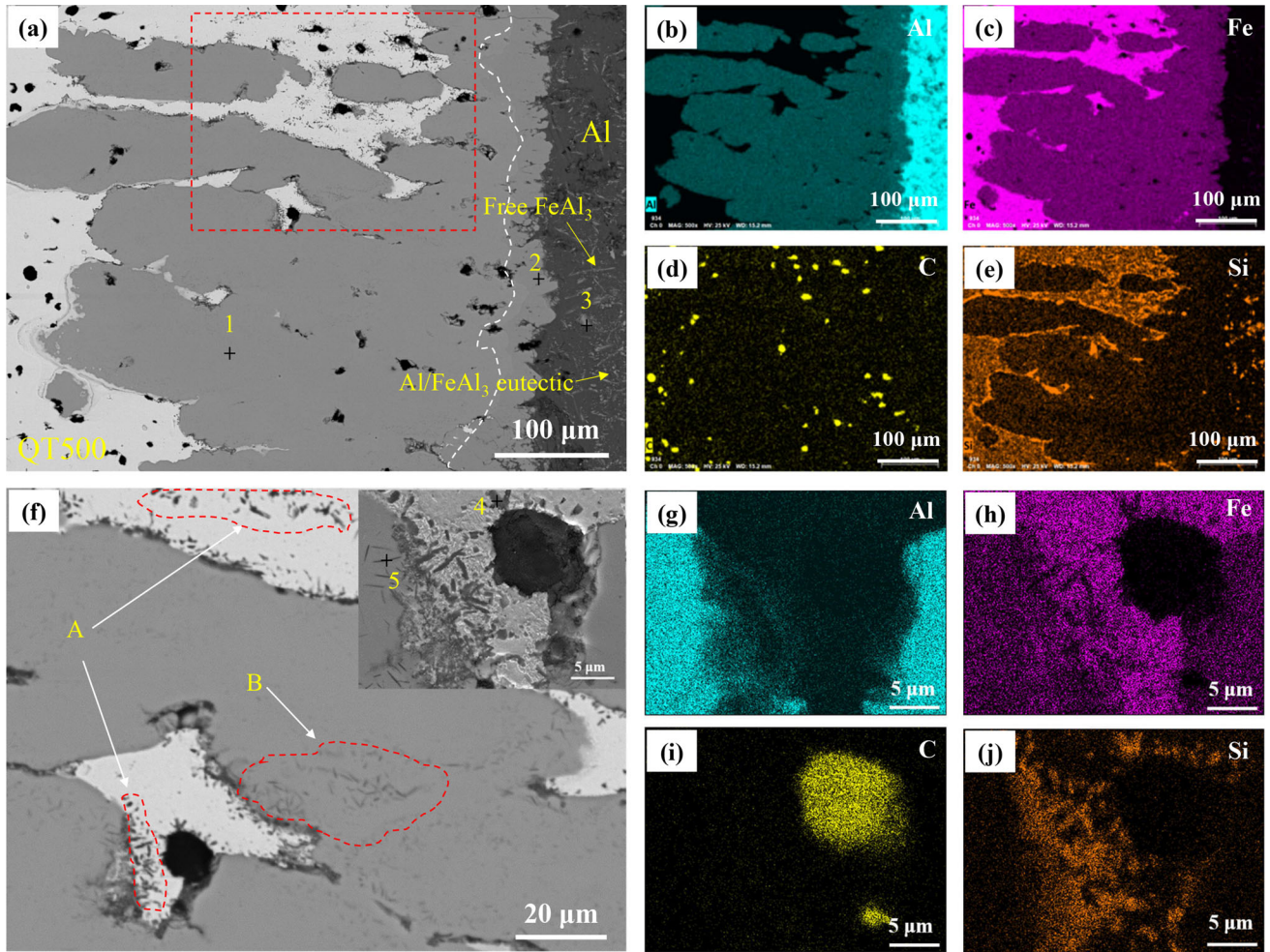

Fig. 6—SEM images and EDS analysis of the corrosion interface formed in QT500 after 24 h in the aluminum melts at 1023 K (750 °C): (*a*) SEM image; (*b*) Al; (*c*) Fe; (*d*) C; (*e*) Si; (*f*) Magnification image; (*g*) Al; (*h*) Fe; (*i*) C; (*j*) Si.

Besides, it is also interesting that a large number of rod-like precipitate phases exist in the red box of Figure 6(a). Figure 6(f) is a magnified image of Figure 6(a), clearly showing the distributions of them. According to their distributions and sizes, they are divided into two types—one is the coarse phase mainly distributed on the matrix, and the other is the fine phase distributed inside the Fe_2Al_5. Combined with EDS (Table III) and the literature,[14,22,23] the coarse one distributed in the matrix may be α-Si formed at high temperature (Area A), while the fine one distributed inside Fe_2Al_5 is Al_4C_3 formed by the combination of C

Table III. Chemical Compositions at the Marked Locations in Fig. 6(a) and (f)

Location	EDS Results (Weight Percent)				Phase Compositions
	Al	Fe	C	Si	
1	53.20	42.42	3.96	0.42	Fe_2Al_5
2	57.10	38.95	3.94	—	$FeAl_3$
3	66.59	29.02	4.39	—	free $FeAl_3$
4	0.63	57.61	3.56	38.20	α-Si
5	62.53	32.99	4.48	—	Al_4C_3

or Fe_3C in the matrix with the diffused Al atoms (Area B). Similar phenomena were observed in the Al-C composites by Etter[24] and Urena.[25] These rod-like precipitate phases effectively inhibited the diffusion of Al atoms into the matrix to some extent. However, since the size of them is too small, their inhibition effect is limited.

Figure 7(a) presents the SEM image of the interfacial morphologies of H13 immersed in aluminum melts at 1023 K (750 °C) for 24 hours. The elements mapping analysis was focused on the yellow box in Figure 6(a). Combined with the EDS analysis (Table IV), it is evident that the IMC layer in H13 is composed of Fe_2Al_5 and $FeAl_3$. A large quantity of acicular and rod-shaped $FeAl_3$ and flocculent eutectics of $FeAl_3$ and aluminum are also found in the solidified aluminum layer. In comparison with the morphologies of $FeAl_3$ in the three ferrous alloys, it can be found that the $FeAl_3$ exfoliating from the IMC layer in HT150 is in block shape, while those of QT500 and H13 are formed in elongated strip and needle shape, respectively. It can be seen from Figure 7(b) that a large number of nano-scale particles are present in the matrix and the IMC layer. Figure 7(b) is a magnified view of the red box in Figure 7(a). Based on the EDS and XRD analysis, they may be nano-carbides formed by the alloying elements including Fe, Cr, V, and Mo in H13. Although the corrosion resistance of H13 is better than that of the iron matrix, the IMC layer in H13 is largest in size among the three ferrous alloys as shown in Figure 2. It implied that the inhibition effect of carbides on aluminum diffusion is much weaker than that of graphite considering their small sizes, limited amounts, and inhomogeneous distributions.

The experimental results demonstrate that the flake graphite in HT150 can inhibit the Al atoms diffusion and thus restrict the IMCs growth most effectively, followed by spheroidal graphite in QT500. Both outperform carbides in H13. Moreover, in comparison with the distribution of Si in the corrosion interface of three ferrous alloys (Figures 5(e), 6(e), and 7(e)), it is found that Si in HT150 is hardly diffused to the solidified aluminum layer, while the diffusion of a large amount of Si into the solidified aluminum layer occurs as shown in Figures 6(e) and 7(e). It also confirms the best diffusion inhibition effect of flake graphite compared with carbides and the spheroidal graphite.

B. Thermodynamic Analysis of the IMC Layer

According to the Fe-Al binary phase diagram, the interactions between iron and aluminum can lead to the formation of IMCs such as FeAl, $FeAl_2$, Fe_2Al_5, and $FeAl_3$. However, for the corrosion of ferrous alloys in aluminum melts, only Fe_2Al_5 and $FeAl_3$ phases usually exist in the interfacial layer. Studies have shown that the formation and growth of IMCs are primarily determined by the growth thermodynamics. The formation possibility of various phases at the interface can be figured out through the Gibbs free energy ΔG of the IMCs, which can be calculated by Reference 26.

$$\Delta G^\theta = \Delta H^\theta_{298\,K} - T\Delta S^\theta_{298\,K}, \qquad [2]$$

where ΔG^θ is the Gibbs free energy of Fe-Al system IMCs under standard conditions, $\Delta H^\theta_{298\,K}$ is the formation enthalpy of Fe-Al system IMCs under standard conditions, $\Delta S^\theta_{298\,K}$ is the entropy change of Fe-Al system IMCs under standard conditions, and T is the thermodynamic temperature.

As the crystallization temperature of the Fe-Al IMCs is above the melting point of aluminum during the corrosion of the ferrous alloy, the Gibbs free energy ΔG of the IMCs is also added to the phase change free energy ΔG^θ_m caused by aluminum melting, which can be determined by

$$\Delta G^\theta = \Delta G^\theta_{Fe-Al} + \Delta G^\theta_m \qquad [3]$$

$$\Delta G^\theta_m = \Delta H^\theta_m - T\Delta S^\theta_m, \qquad [4]$$

where ΔG^θ_{Fe-Al} is the Gibbs free energy of Fe-Al compound under standard conditions, ΔG^θ_m is the Gibbs free energy change of Fe-Al compound after aluminum melting, ΔH^θ_m is the enthalpy change during aluminum melting, and ΔS^θ_m is the entropy change during aluminum melting.

In terms of the ferrous alloys immersed in the aluminum melts, it is assumed that Al atoms are sufficient for Fe atoms to bond with, and therefore the IMC formation is determined by the Gibbs free energy of per mole of Fe atom compound. According to the thermodynamic data,[26–28] the Gibbs free energy of per mole of Fe atom compound can be given by

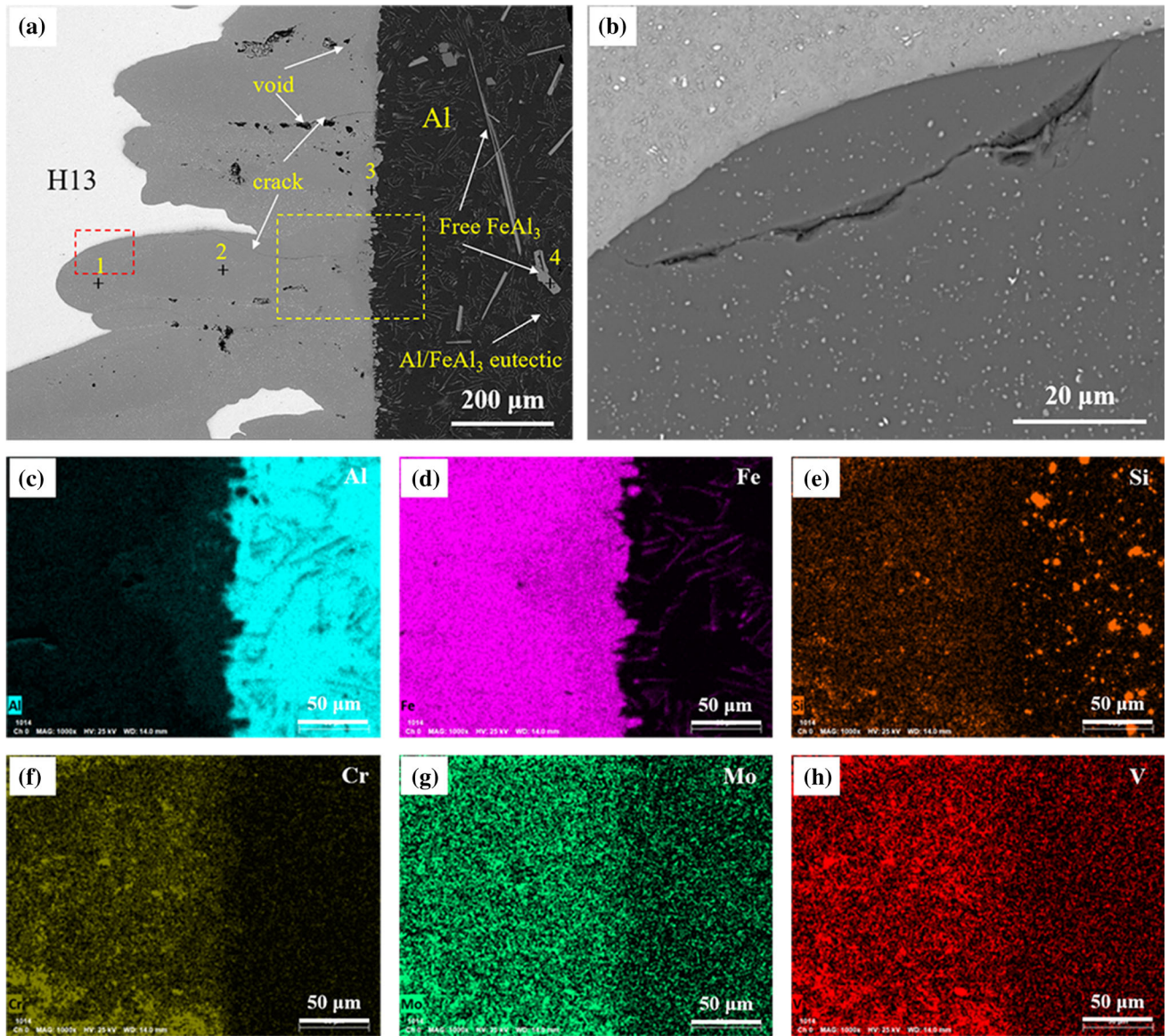$$\Delta G^\theta_{FeAl_3} = -142770 + 50.58T \qquad [5]$$

Fig. 7—SEM images and EDS analysis of the corrosion interface formed in H13 after 24 h in the aluminum melts at 1023 K (750 °C): (*a*) SEM image; (*b*) Magnification image; (*c*) Al; (*d*) Fe; (*e*) Si; (*f*) Cr; (*g*) Mo; (*h*) V.

Table IV. Chemical Compositions at the Marked Locations in Fig. 7(a)

Location	EDS Results (Weight Percent)						Phase Compositions
	Al	Fe	C	Cr	V	Mo	
1	49.35	42.75	4.04	2.71	0.92	0.23	$(FeM)_xC_y$
2	50.41	44.33	4.08	1.18	—	—	Fe_2Al_5
3	57.13	37.65	4.30	0.92	—	—	$FeAl_3$
4	61.50	32.81	4.38	1.32	—	—	free $FeAl_3$

$$\Delta G^{\theta}_{FeAl_{2.5}} = -126985.5 + 42.96T \qquad [6]$$

$$\Delta G^{\theta}_{FeAl_2} = -102577 + 33.20T \qquad [7]$$

$$\Delta G^{\theta}_{FeAl} = -58950 + 15.99T. \qquad [8]$$

As shown in Figure 8, when the aluminum content increases, ΔG^{θ} of the compounds gradually decreases.

When the aluminum content reaches the maximum, the compound has the minimum ΔG^θ. At the temperature of 1023 K (750 °C), $\Delta G^\theta_{FeAl_3} < \Delta G^\theta_{FeAl_{2.5}} < \Delta G^\theta_{FeAl_2} < \Delta G^\theta_{FeAl}$. The Fe-Al IMC that is most likely to be formed during the corrosion of ferrous alloys in aluminum melts should be FeAl$_3$ phase, followed by Fe$_2$Al$_5$, FeAl$_2$, and FeAl phases. Among them, FeAl$_2$ phase is a metastable phase that cannot exit stably, and FeAl is also hardly to be formed owing to the limited amount of Fe at the interface.[29] The thermodynamic analysis of the IMC formation is carried out based on the equilibrium conditions, and the calculation results can only reflect the IMC formation possibility. However, the corrosion of ferrous alloys in aluminum melts is a dynamic non-equilibrium process, and the formation of IMCs is also dependent on the factors including interface reaction temperature and reaction time. Therefore, the kinetics analysis of the interface reaction is necessary.
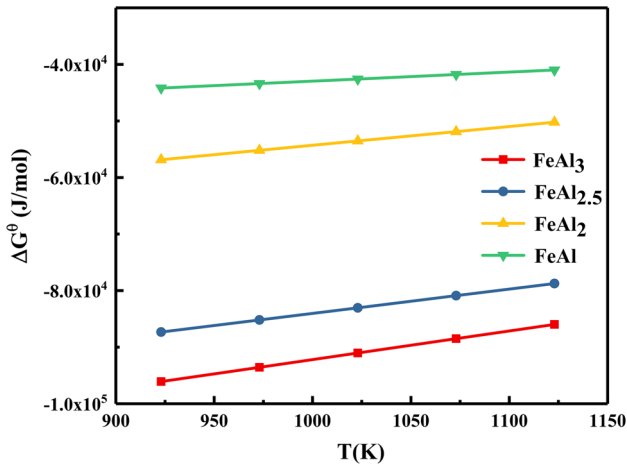

Fig. 8—Variation of ΔG^θ of Fe-Al IMCs with different temperatures.

C. Growth Kinetics of the IMC Layer

A kinetics model, which is an extension of T-L-K model[30] to the situation of ferrous alloys where carbon element exists in different forms, is first proposed to quantitatively account for the corrosion behavior of ferrous alloys in the static aluminum melts by making the following assumptions: (1) Due to the narrow composition range of IMCs, the interdiffusion coefficient is taken to be independent of the composition. (2) The concentration gradient of Al in IMC layer is independent of position. As illustrated in Figure 9, the ferrous alloy is immersed in the aluminum melts until it is wetted entirely (Figure 9(a)). After a period of time, a transition layer of IMC is formed at the solid–liquid interface (Figure 9(b)). At the interface I between the matrix and the IMC layer, Al atoms that diffused through the IMCs layer could react with the matrix, and then more IMCs could be formed. The consumption of the matrix caused the interface I to proceed continuously into the interior of the matrix and led to an increase in the thickness of the IMC layer and thus the corrosion of the matrix. In the meanwhile, the dissolution of IMCs occurs continuously at the interface II near the aluminum melts, so that the interface II moves continuously towards the matrix. Therefore, it is assumed that the thickness (L) of the IMC layer is dominated by the growth and dissolution of IMCs.

The diffusion flux perpendicular to the interface can be expressed by Fick's law[31]:

$$J = -D \frac{dC}{dX} \qquad [9]$$

where J is the diffusion flux of the Al atoms, C is the concentration of Al in the IMC layer, D is the interdiffusion coefficient of the IMCs, x is the position in the normal direction of diffusion, and minus sign (−)
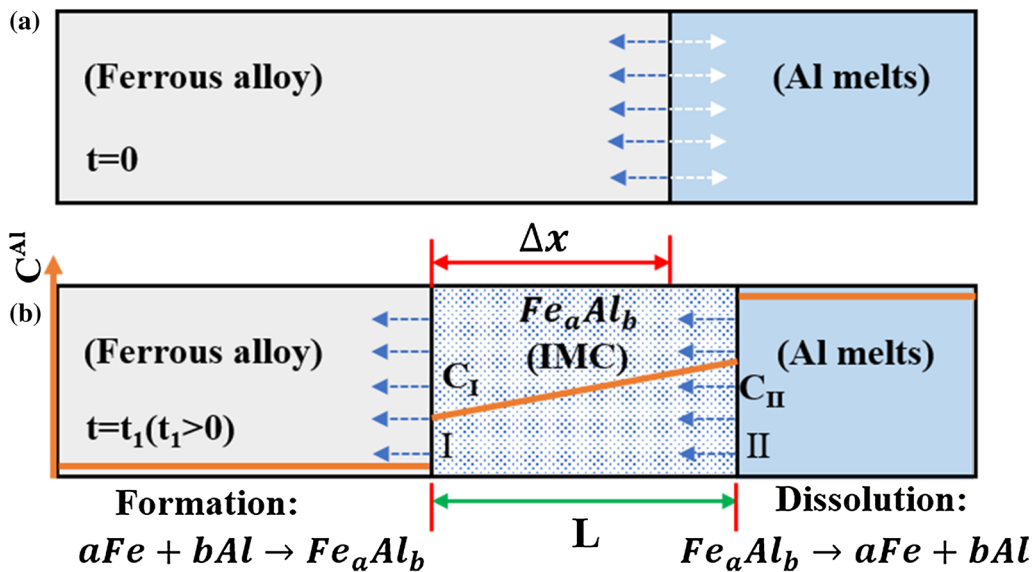

Fig. 9—Schematic of the interfacial reaction between ferrous alloy and Al melts: (a) $t = 0$, ferrous alloy and Al melts just contacted with each other; (b) $t = t_1$ ($t_1 > 0$), at interface I, ferrous alloy has reacted with Al atoms diffused through the layer to form Fe$_a$Al$_b$. At interface II, Fe$_a$Al$_b$ has dissolved into the Al melts.

indicates that the direction of the diffusion flow is opposite to the direction of the concentration gradient.

In this model, the concentration gradient of Al in the IMC layer is considered to be independent of position, and then

$$\frac{dC}{dX} = \frac{C_I - C_{II}}{L}, \quad [10]$$

where C_I and C_{II} are the concentration of Al at the interface I and II, respectively. To quantitatively estimate the extent to which the existence of carbon can influence the diffusion of aluminum to the matrix, the diffusion inhibition factor λ is introduced. By substituting Eq. [10] into Eq. [9] and rearranging, one has

$$J = \frac{D}{\lambda} \frac{C_{II} - C_I}{L}. \quad [11]$$

During the corrosion of the ferrous alloy in the aluminum melts, if the thickness of the newly formed IMCs in a duration dt is defined as dL_g, then the relationship between dL_g and dt is given by

$$JSdt = \frac{b\rho_{IMC}SdL_g}{W_{IMC}} = \frac{D}{\lambda} \frac{C_{II} - C_I}{L} Sdt, \quad [12]$$

where t is the corrosion time, b is the stoichiometric ratio of Al in the IMC (Fe$_a$Al$_b$), ρ_{IMC} is the density of the IMC, S is the area of the IMCs in contact with the aluminum melts, L_g is the thickness of the IMC, and W_{IMC} is the molar mass of the IMC. Then, the growth rate of the IMC can be given by

$$\frac{dL_g}{dt} = \frac{DW_{IMC}(C_{II} - C_I)}{\lambda b\rho_{IMC}L}. \quad [13]$$

In interface II, the dissolution of IMCs into aluminum melts can be described by the Nernst–Shchukarev equation[32]:

$$\frac{dC}{dt} = K\frac{S}{V}(C_S - C), \quad [14]$$

where C is the concentration of Fe in the aluminum melts, K is the dissolution rate constant, S is the area of the IMCs in contact with the aluminum melts, V is the volume of the aluminum melts, and C_S is the saturation concentration of Fe in the aluminum melts. During the time dt, the thickness dL_d of the IMCs is dissolved, and the concentration of Fe in the aluminum melts is increased by dC, which can be described by

$$dC = \frac{\rho_{IMC}SdL_d}{W_{IMC}}\frac{a}{V}, \quad [15]$$

where a is the stoichiometric ratio of Fe in the IMC (Fe$_a$Al$_b$).

Under an initial condition: $t = 0$, $C = 0$,

$$C = C_S\left(1 - e^{-\frac{KS}{V}t}\right). \quad [16]$$

Then, the dissolution rate of the IMCs is determined by

$$\frac{dL_d}{dt} = \frac{W_{IMC}V}{\rho_{IMC}aS}K\frac{S}{V}(C_{II} - C_I) = \frac{C_SKW_{IMC}}{\rho_{IMC}a}e^{-\frac{KS}{V}t}. \quad [17]$$

Given the volume V of the aluminum melts is sufficiently large, the value of S/V is almost close to 0, so that

$$\frac{dL_d}{dt} = \frac{C_SKW_{IMC}}{\rho_{IMC}a}. \quad [18]$$

Since the thickness of the IMC layer is determined by its growth and dissolution, the variation rate of the IMC layer thickness is given by

$$\frac{dL}{dt} = \frac{dL_g}{dt} - \frac{dL_d}{dt} = \frac{DW_{IMC}(C_{II} - C_I)}{\lambda b\rho_{IMC}L} - \frac{C_SKW_{IMC}}{\rho_{IMC}a}. \quad [19]$$

When $\frac{dL}{dt} = 0$, the growth and dissolution of IMCs reach an equilibrium state. Thus,

$$L_{max} = \frac{D(C_{II} - C_I)a}{\lambda C_S Kb}, \quad [20]$$

where L_{max} is the maximum thickness of the IMC layer.

In this model, the corrosion of ferrous alloy matrix is accompanied by the growth of IMCs. At the time of dt, the thickness of the IMC layer is increased by dL_g, and the corrosion rate of the matrix d$(\Delta x)/dt$ can be calculated by

$$\frac{d(\Delta x)}{dt} = \frac{a\rho_{IMC}W_{Fe}}{\rho_{Fe}W_{IMC}}\frac{dL_g}{dt} = \frac{aW_{Fe}D(C_{II} - C_I)}{\lambda b\rho_{Fe}L}, \quad [21]$$

where ρ_{Fe} is the density of Fe and W_{Fe} is the molar mass of Fe. When the corrosion of ferrous alloy is initiated, the thickness of the IMC layer is so small that $\frac{dL_g}{dt} \gg \frac{dL_d}{dt}$. Hence,

$$\frac{dL}{dt} = \frac{dL_g}{dt} - \frac{dL_d}{dt} \approx \frac{dL_g}{dt}. \quad [22]$$

Under an initial condition: $t = 0$, $L = 0$,

$$L = \sqrt{\frac{2W_{IMC}D(C_{II} - C_I)}{\lambda b\rho_{IMC}}}\sqrt{t}. \quad [23]$$

Then

$$\frac{d(\Delta x)}{dt} = \frac{aW_{Fe}}{\rho_{Fe}}\sqrt{\frac{\rho_{IMC}D(C_{II} - C_I)}{2\lambda bW_{IMC}}}\frac{1}{\sqrt{t}} \quad [24]$$

$$\Delta x = \frac{aW_{Fe}}{\rho_{Fe}}\sqrt{\frac{2\rho_{IMC}D(C_{II} - C_I)}{\lambda bW_{IMC}}}\sqrt{t}. \quad [25]$$

The IMC layer formed by the reactions between the ferrous alloy and the aluminum melts is quantitatively analyzed, and the experimental and calculation results are compared and shown in Figure 10. The comparison of L_{max} for the Fe matrix and the three ferrous alloys is shown in Figure 10(a). The Fe matrix exhibits the largest L_{max} as no diffusion inhibitor is considered, whereas H150 the smallest one as the flake graphite may serve as the most effective diffusion inhibitor. The diffusion inhibition factor λ is introduced in this work in order to quantitatively estimate the contribution of carbon existence forms to the diffusion inhibition and thus the growth restriction of IMCs. For the α-Fe matrix, the value of λ is equal to 1. The corresponding values of λ is obtained by substituting the measured L_{max} of the three ferrous alloys into Eq. [20]. As illustrated in Figure 10(b), H150 has the largest value of λ among the three ferrous alloys, indicating the most effective diffusion inhibition, which is in accordance with the experimental observation. More importantly, the

diffusion inhibition factor λ essentially mirrors the corrosion resistance of ferrous alloys in the aluminum melts. The higher is λ, the stronger the corrosion resistance of the ferrous alloy. From Eq. [24], it can be seen that the corrosion rate is inversely proportional to $\lambda^{1/2}$. The λ value corresponding to the three ferrous alloys is substituted into Eq. [25], and the variation of matrix thickness loss Δx with time t is plotted in Figure 10(c). The variation trend of the measured Δx of the three ferrous alloys is consistent with the theoretical model. The parameters used in this model are listed in Table V.

In reality, the thickness of the IMC layer is not only determined by its growth and dissolution rate, but also by the exfoliation of the IMC layer caused by the thermal stress. Rezaei et al.[35] found that microcracks generated inside the IMC layer can accelerate the fracture of the IMC layer and promote the diffusion of Al atoms into the metal matrix. Besides, the reaction between aluminum melts and the ferrous alloy is
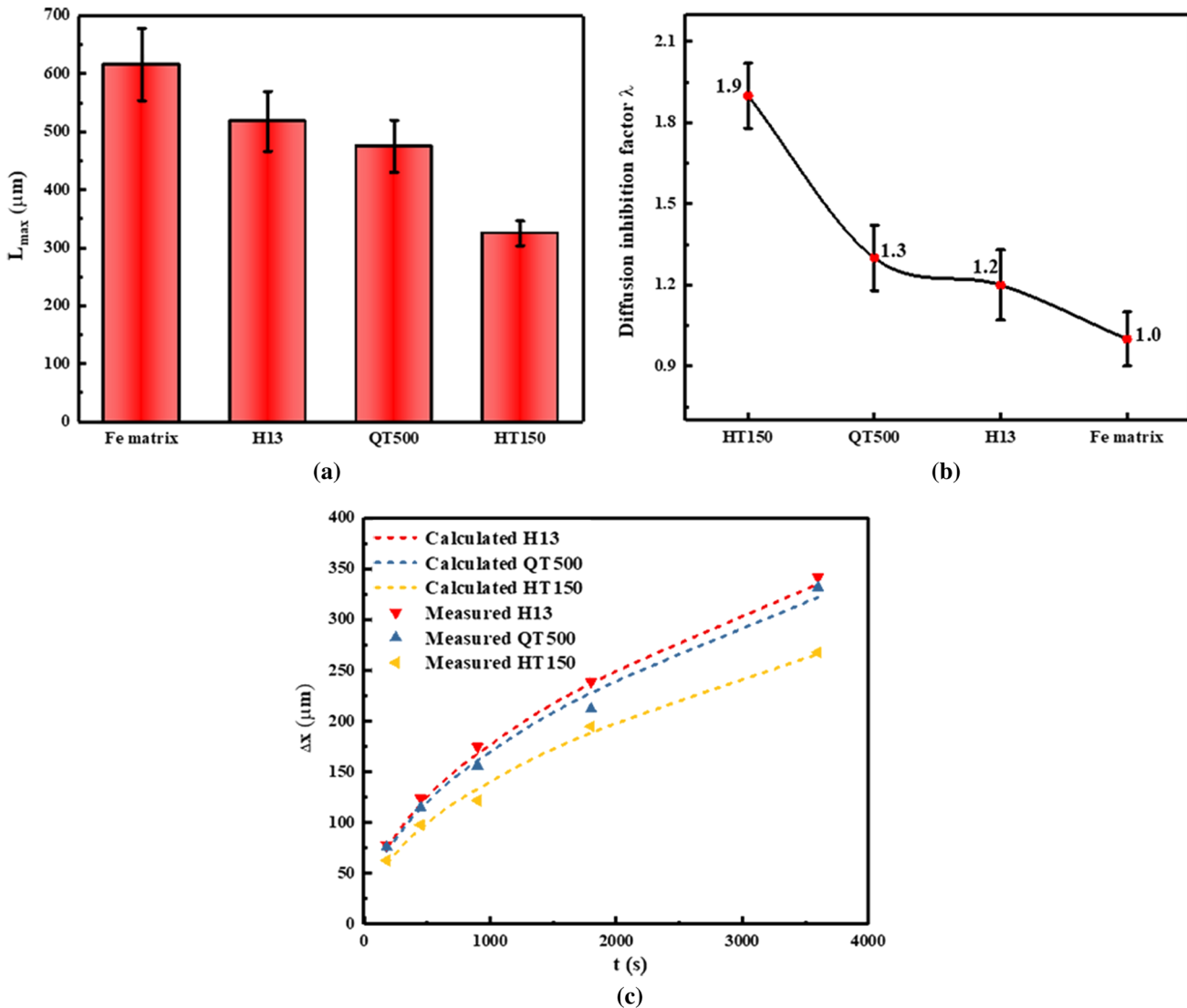

Fig. 10—(a) Maximum thickness of IMC layers next to ferrous alloys; (b) the value of λ for the three ferrous alloys; (c) matrix thickness loss of ferrous alloys vs immersion time.

Table V. Parameters for Calculations for the Solid Iron-Aluminum Melt Reaction System

| Parameter	Unit	Description	1023 K (750 °C)	Remark
W_{IMC}	kg/mol	molar mass of the IMC	2.47×10^{-1}	this work
W_{Fe}	kg/mol	molar mass of the Fe	5.59×10^{-2}	this work
ρ_{IMC}	kg/m^3	density of the IMC	4.1×10^3	32
ρ_{Fe}	kg/m^3	density of the Fe	7.86×10^3	33
C_{II}–C_I	mol/m^3	concentration gradient of Al between the interface II and I	8×10^3	13
C_S	mol/m^3	saturation concentration of Fe in the aluminum melts	1.07×10^3	32
K	m/s	dissolution rate constant	1.69×10^{-5}	34
D	m^2/s	interdiffusion coefficient of the IMCs	3.9×10^{-9}	34
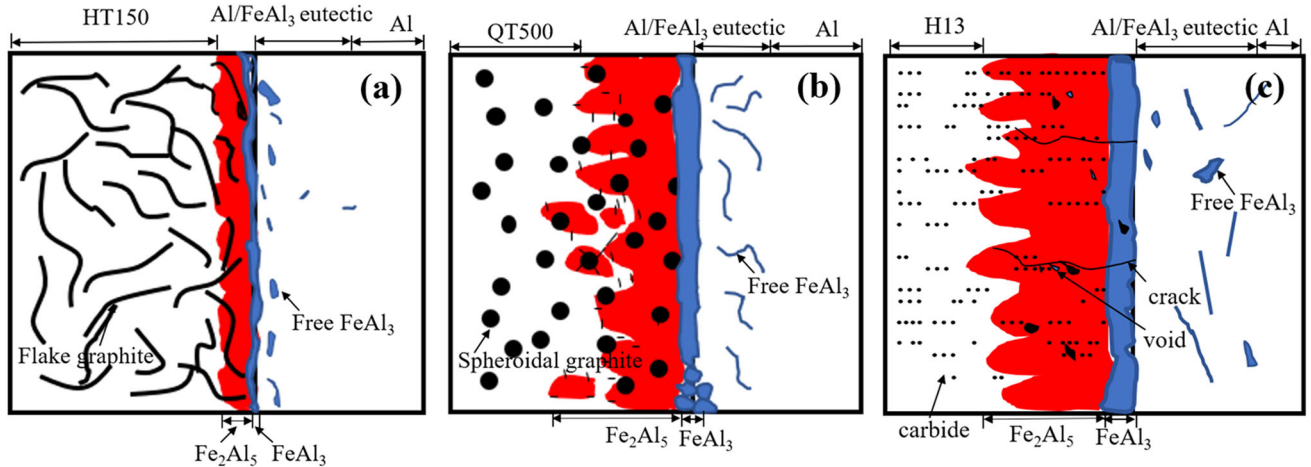
Fig. 11—Illustration of the corrosion mechanism for the three ferrous alloys: (*a*) HT150; (*b*) QT500; (*c*) H13.

exothermic, and the generated heat will cause an increase in the temperature at the Al/IMC interface, while the temperature of aluminum melts itself is constant. Therefore, there is a certain temperature gradient between the higher temperature Al/IMC interface and the aluminum melts. The heat will be transferred to the aluminum melts through the IMC layer. Influenced by the heat flow, the IMCs with microcracks tend to exfoliate, then flow into the aluminum melts, and finally dissolve.[36]

Figure 11 is the schematic of the corrosion mechanism for the three ferrous alloys. The barrier effect of graphite on Al melts is closely related to its morphology. Spheroidal graphite exists in the matrix in isolation, and the distance among them is relatively large, so the effective barrier area of the Al melt diffusion is limited. The spheroidal graphite is detached from the matrix and distributed discretely in the IMC layer and solidified aluminum layer, which seems to contribute less to the diffusion inhibition of Al atoms in the matrix. Thus, the formation of the IMC layer cannot be slowed down. The inhibition effect of carbides on aluminum diffusion is much weaker than that of graphite considering their small size, limited amount, and inhomogeneous distribution as shown in Figure 11(c). Compared with the spheroidal graphite and nano-carbide, the flake graphite is distributed in the network form and the distance between

them is relatively small, which inhibits the diffusion of Al atoms to the IMC layer more effectively. Moreover, the graphite network can also act as the skeleton reinforcement to enhance the bonding strength between the matrix and the IMC layer and hinder the exfoliation and dissolution of IMCs more effectively thus resulting in more excellent corrosion resistance of HT150.

IV. CONCLUSIONS

1. The IMC layer formed by the ferrous alloy and the aluminum melts is composed of Fe$_2$Al$_5$ and FeAl$_3$.
2. The flake graphite in HT150 can reduce the corrosion rate most effectively, followed by spheroidal graphite in QT500, and least by carbide in H13.
3. The relationship between the corrosion rate of the ferrous alloy and the diffusion inhibition factor λ is established and given by $\frac{d(\Delta x)}{dt} = \frac{aW_{Fe}}{\rho_{Fe}} \sqrt{\frac{\rho_{IMC}D(C_{II}-C_I)}{2\lambda bW_{IMC}}} \frac{1}{\sqrt{t}}$.
4. The theoretical analysis demonstrates that the diffusion inhibition factor λ essentially mirrors the corrosion resistance of ferrous alloys in the aluminum melts, and the higher is λ, the stronger the corrosion resistance of the ferrous alloy.

REFERENCES

1. H. Yang, W.T. Tsai, J.C. Kuo, and C. Yang: *J. Alloys Compd.*, 2011, vol. 509, pp. 8176–82.
2. V. Nunes, F.J.G. Silva, M.F. Andrade, R. Alexandre, and A.P.M. Baptista: *Surf. Coat. Technol.*, 2017, vol. 332, pp. 319–31.
3. N.L. Okamoto, J. Okumura, M. Higashi, and H. Inui: *Acta Mater.*, 2017, vol. 129, pp. 290–99.
4. M. Yousaf, J. Iqbal, and M. Ajmal: *Mater. Charact.*, 2011, vol. 62, pp. 517–25.
5. X. Zhang, W. Chen, H. Luo, S. Li, T. Zhou, and L. Shi: *Corros. Sci.*, 2017, vol. 125, pp. 20–28.
6. D. Alonso-Peña, M.E. Arnáiz-García, J.L. Valero-Gasalla, A.M. Arnáiz-García, R. Campillo-Campaña, J. Alonso-Peña, J.M. González-Santos, A.L. Fernández-Díaz, and J. Arnáiz: *Burns*, 2015, vol. 41, pp. 1122–25.
7. S. Komarov and D. Kuznetsov: *Int. J. Refract. Met. Hard Mater.*, 2012, vol. 35, pp. 76–83.
8. N. Tunca, G.W. Delamore, and R.W. Smith: *Metall. Mater. Trans. A*, 1990, vol. 21A, pp. 2919–28.
9. N. Tang, Y.P. Li, S. Kurosu, H. Matsumoto, and A. Chiba: *Corros. Sci.*, 2012, vol. 60, pp. 32–37.
10. Y. Li, N. Tang, P. Tunthawiroon, Y. Koizumi and A. chiba: Corros. Sci., 2013, vol. 73, pp. 72-79.
11. H. Xiao, W. Chen, and Z. Liu: *Trans. Nonferrous Met. Soc. China*, 2012, vol. 22, pp. 2320–26.
12. M.B. Lin, C.J. Wang, and A.A. Volinsky: *Surf. Coat. Technol.*, 2011, vol. 206, pp. 1595–99.
13. D. Cong, H. Zhou, Z. Ren, H. Zhang, L. Ren, C. Meng, and C. Wang: *Opt. Laser. Eng.*, 2014, vol. 54, pp. 55–61.
14. M.S. Sidhu: PhD thesis, University of Canterbury, 2012.
15. D. Balloy, J.C. Tissier, M.L. Giorgi, M.L. Giorgi, and M. Briant: *Metall. Mater. Trans. A*, 2010, vol. 41, pp. 2366–76.
16. J. Rong, Z. Kang, S. Chen, D. Yang, J. Huang, and J. Yang: *Mater. Charact.*, 2017, vol. 132, pp. 413–21.
17. A.V. Alboom, B. Lemmens, B. Breitbach, E.D. Grave, S. Cottenier, and K. Verbeken: *Surf. Coat. Technol.*, 2017, vol. 324, pp. 419–28.
18. Z. Ding, Q. Hu, W. Lu, X. Ge, S. Gao, S. Sun, T. Yang, M. Xia, and J. Li: *Mater. Charact.*, 2018, vol. 136, pp. 157–64.
19. K. Bouche, F. Barbier, and A. Coulet: *Mater. Sci. Eng. A*, 1998, vol. 249, pp. 167–75.
20. T. Heumann and S. Dittrich: *Z. Metall.*, 1959, vol. 50, pp. 617–25.
21. S. Chen, D. Yang, M. Zhang, J. Huang, and X. Zhao: *Metall. Mater. Trans. A*, 2016, vol. 47A, pp. 5088–100.
22. M.S. Sidhu, C.M. Bishop, and M.V. Kral: *Int. J. Cast Met. Res.*, 2014, vol. 27, pp. 321–28.
23. H. Springer, A. Kostka, E.J. Payton, D. Raabe, A. Kaysser-Pyzalla, and G. Eggeler: *Acta Mater.*, 2011, vol. 59, pp. 1586–600.
24. T. Etter, P. Schulz, M. Weber, J. Metz, M. Wimmler, J.F. Löffler, and P.J. Uggowitzer: *Mater. Sci. Eng. A*, 2007, vol. 448, pp. 1–6.
25. A. Ureña, J. Rams, M.D. Escalera, and M. Sánchez: *Compos. Sci. Technol.*, 2005, vol. 65, pp. 2025–38.
26. B. Liu: *Hot Dip Aluminizing of Steel*, Metallurgical Industry Press, Beijing, 1995, pp. 21–23.
27. G. Wang, A. Meng, and Z. Ren: *Physical Chemistry*, 3rd ed., Shanghai Scientific & Technical Publishers, Shanghai, 2007, pp. 293–302.
28. S. Mei, M. Gao, J. Yan, C. Zhang, G. Li, and X. Zeng: *Sci. Technol. Weld. Join.*, 2013, vol. 18 (4), pp. 293–300.
29. R.W. Richards, R.D. Jones, P.D. Clements, and H. Clarke: *Int. Mater. Rev.*, 1994, vol. 39, pp. 191–212.
30. N. Tang, Y. Li, Y. Koizumi, S. Kurosu, and A. Chiba: *Corros. Sci.*, 2013, vol. 73, pp. 54–61.
31. L.L. Bircumshaw and A.C. Riddiford: *Q. Rev. Chem. Soc.*, 1952, vol. 6, pp. 157–85.
32. V.N. Yeremenko, Y.V. Natanzon, and V.I. Dybkiv: *J. Mater. Sci.*, 1981, vol. 16, pp. 1748–56.
33. J.R. Davis: *Metals Handbook*, Desk ed., ASM, USA, 1998.
34. V.N. Eremenko, Y.V. Natanzon, and V.I. Dybkov: *J. Mater. Sci.*, 1985, vol. 20, pp. 501–07.
35. H. Rezaei, M.R. Akbarpour, and H.R. Shahverdi: *JOM*, 2015, vol. 67, pp. 1443–50.
36. J. Mackowiak and L.L. Shreir: *J. Less Common Met.*, 1959, vol. 1 (6), pp. 456–66.